CCFE
CULHAM CENTRE FOR FUSION ENERGY

UK Atomic Energy Authority

UKAEA-CCFE-PR(25)335

A. M. Patel, N. C. Hawkes, M. O'Mullane, K.-D. Zastrow

X-ray spectrometer configuration, throughput and data treatment over the JET DTE2 and DTE3 Camapigns

X-ray spectrometer configuration, throughput and data treatment over the JET DTE2 and DTE3 Camapigns

A. M. Patel, N. C. Hawkes, M. O'Mullane, K.-D. Zastrow

This is a preprint of a paper submitted for publication in
Review of Scientific Instruments

X-ray crystal spectrometer throughput, data treatment and configuration over the JET DTE2 and DTE3 Campaigns

A. M. Patel,† N. C. Hawkes, and K.-D. Zastrow

United Kingdom Atomic Energy Authority, Culham Campus, Abingdon, Oxfordshire, OX14 3DB, UK

M. O'Mullane

Department of Physics, University of Strathclyde, Glasgow, G1 1XJ, UK

JET contributors

See author list of: "Overview of T and DT results in JET with ITER-like wall" by C.F. Maggi et al. Nuclear Fusion **64** *112012*

The EUROfusion Tokamak Exploitation Team

See author list of: "Overview of the EUROfusion Tokamak Exploitation programme in support of ITER and DEMO" by E. Joffrin, et al. Nucl. Fusion **64** *112019*

The calibration of the JET x-ray spectrometer is presented. The absolute throughput, diffractor focussing and instrument function of the spectrometer is presented and the quality of the ion temperature measurement is re-assessed, particularly at the lower end. The addition of a second diffractor enables simultaneous measurements of the spectra from H- and He-like nickel which widens the spatial coverage of the core-ion temperature measurements for high-performance plasmas at a fixed Bragg angle range.

A calculation of the absolute continua from the spectrum background from the second diffractor is analysed for different JET plasmas. The spectrometer's narrow bandwidth makes it ideal as an "x-ray monochromator" that can sample a single energy channel (or two over the two crystal orders) within the free-free and free-bound x-ray continua. The measurable effect for impurity-seeded plasmas is explored as a means to determine the plasma concentration of the seeding impurities which has the potential to be a robust method for high performance DT operations in reactor-class machines.

†Electronic address: ash.patel@ukaea.uk

INTRODUCTION

The JET facility [1] is a tokamak plasma where the ion temperatures have exceeded 10keV over the core region during deuterium-tritium operations in the DTE2 and DTE3 Campaigns [2, 3]. Resonance line emission of H- and He-like ions of the intrinsic impurity nickel emit in the 1-2Å wavelength region and these spectra are rich in satellite lines on the long wavelength side of the resonance lines [4, 5]. Doppler-broadened line profiles and absolute intensities along with high-resolution spectral measurements are an important way to evaluate local electron temperatures, impurity ion temperature and their concentrations as well as an ionization equilibrium determination [6].

The x-ray spectrometer deployed in JET since inception [7] is in the Johann configuration [8] with a large Rowland circle diameter resulting in ∼20m long beam lines converging onto a crystal-diffraction chamber box. The optical axis, at the centre of the field of view, is tangential to the inner vacuum-vessel wall as shown in the general layout in FIG. 1. The principal advantages of a very large diameter include negligible optical aberrations of the cylindrically bent diffractor, good wavelength resolution and the ability to separate the detector from noise and damage by isolating the sensor from the plasma both by distance and by locating it behind the biological shield-wall. The Si/Ge diffractor damage over JET campaigns is negligible due to its location and low neutron dose [9]. However for reactor-class machines, a planer pre-disperser that has a high threshold, e.g. for neutron damage, will be required to deflect required x-ray energies to crystal spectrometers [10]. Further details on upgrades to the original spectrometer, including the introduction of a second parallel, independent spectrometer system, large-area three-stage gas electron multiplier sensors, new data acquisition systems, high-definition diffractor and arm motion control are summarised in [11].

The profile of the emission from a spectral line of an ion is determined by the electron temperature and density profiles and by cross-field impurity transport and plasma rotation. For emission arising in the core region, i.e. $r/a < 0.6$, the latter effects are small and ionization

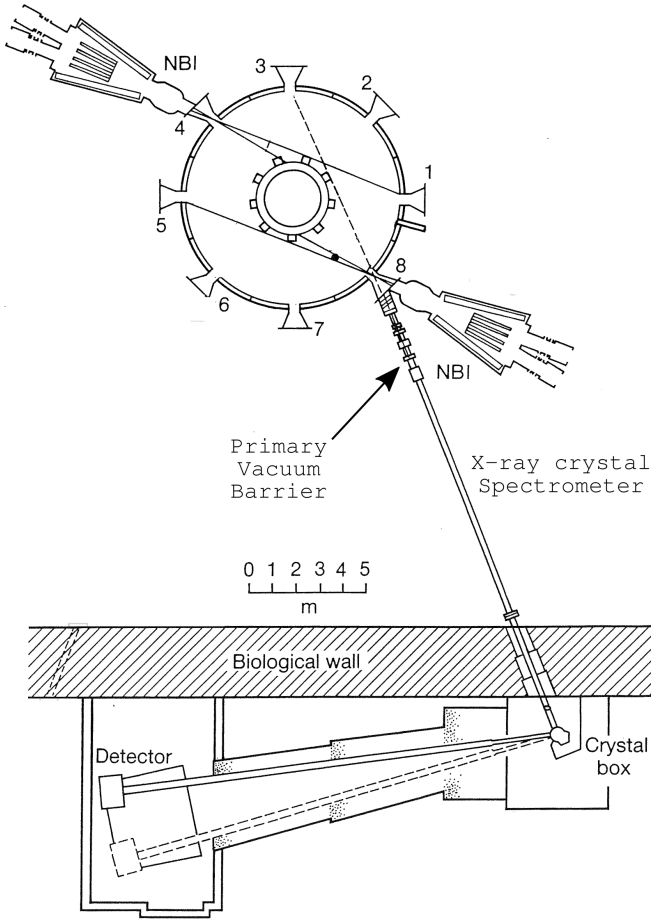

FIG. 1: Layout of the high-resolution x-ray crystal spectrometer at the JET facility. Neutral Beam Injection (NBI) systems are also shown.

equilibrium between ion stages may be assumed. The ionization potentials of Ni^{25+}, Ni^{26+} and Ni^{27+} (Li-, He- and H-like Ni) are 2.4keV, 10.3keV and 10.7keV respectively leading to a wide He-like Ni profile for most JET discharges which have central electron temperatures in the 2-5keV range. H-like ions are only seen in higher performance, and higher central electron temperature, plasmas. The JET x-ray spectrometer measures line-integrated and background emissivity along the line of sight so any localisation must be modelled.

The paper is organised into sections detailing the instrument, its configuration, tolerances and sensitivity with a section on interpreting the line and continuum emission in hydrogenic, helium and impurity-seeded plasmas. Absolute continua analysis as detailed here may complement other quantitative measurements in existing and future reactor-class machines such as ITER [12] where diagnostics are challenged with plasma-facing optics degradation from material deposition, damage due to neutron irradiation [13, 14] and will have to limit or mitigate with design considerations [15].

Instrument detail

The two spectrometers are parallel and stacked vertically, inclined such that the respective optical-axes from the sensor and crystal meet at a small angle, at the centre of the primary vacuum barrier (See FIG. 1). This consists of a beryllium foil supported by a grid structure - at the Rowland circle - which is capable of withstanding a pressure differential of up to an atmosphere and separates the torus vacuum from the spectrometer vacuum which is normally maintained at $\sim 10^{-4}$mbar.

TABLE I details the wavelength ranges and diffractor integrated reflectivities, R_c, for the Ge and Si crystal-based spectrometers. Using the He-like spectral feature, comprising of the "w" resonance line at 1.5884A and satellite lines, to measure ion temperatures is the primary purpose of the instrument and data is available for the majority of JET discharges. The H-like Ni-Ly_{α_1} (1.5303Å) is

Crystal	Order	2d Å	λ_{min} Å	λ_{max} Å	R_c μrad	$R_c/(R_c$ Ge440)
Si	1	3.840312	3.042	3.066	56	2.6
	2		1.521	1.533	8.9	0.41
	3		1.014	1.022	1.8	0.08
Ge	1	3.9954	3.170	3.194	134	6.3
	2		1.585	1.597	21.4	$\equiv 1$
	3		1.057	1.065	4.37	0.20

TABLE I: Sensor wavelength ranges covered with the installed Si and Ge diffractors at a Bragg angle of $\sim 52.67°$ at 1.5884Å. H- and He-like Ni Ly_{α_1} and "w" lines are of primary interest for ion-temperature. R_c is the diffractor integrated reflectivity.

measured by the new Si diffractor. The measured emission will at most be 20% of the He-like "w" resonance line from the Ge crystal assuming similar spatial emission profiles - here the 41% drop in the Si diffractor reflectivity is compounded with the fact that light from only a single plasma-pass is made due to vignetting hence the signal to noise levels will be poorer for the H-like stage (see sections on throughput and vignetting). However fitting the line shape, including accounting for the satellite lines contribution, gives a good measure of the ion temperature averaged over the spatial profile of the respective ion stages. These, effectively independent, spectrometer systems which extend the ion temperature range but also have some overlap is the motivation for adding the Si diffractor.

Pulse-height (energy-resolved) sensor data for both spectrometers is shown in FIG. 2. Spectra that contain the H- and He-like Ni emissions are isolated at the 2^{nd} order, He-like signals are especially strong which lead to good ion temperature estimates from line-fitting as well as being well time-resolved. This short wavelength part of the spectra with the highest signal levels is the "main-stay" of the system. The Ge diffractor, a spectral band-pass encompasses the He- like Ni spectra in the 1.585-1.597Å

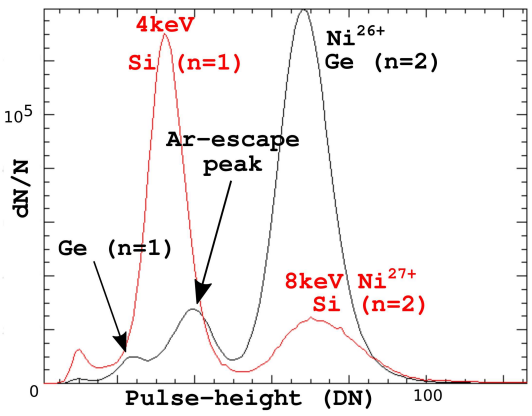

FIG. 2: Typical pulse-height distributions from the two spectrometers (JET #99360) - both Ni emissions are selected from the 2^{nd} order spectra. Si diffractor data are shown in red - Mylar attenuators are used to reduce the first orders such that the overall count rates are comfortably within sensor saturation limits. The n=3 signals are negligible.

wavelength region.
The remainder of this section will outline the methods for the laboratory focussing of both diffractors prior to DTE2 and DTE3 Campaigns, vignetting at the centre of the field of view and instrument throughput.

Diffractor bend quality

The large focal length places the diffractors and sensors outside the torus hall. The radius of curvature of the crystal laminae is $\sim$ 25m which places strict requirements on the quality of the material and on the accuracy when preparing the diffractor [16]. The crystal dimensions are 230x35x5mm and are cut parallel to the 220 plane for both the Ge and Si plates. As discussed in [16], focussing the crystal in visible light is transferable to the x-ray domain so no other procedure is required to quantify the contribution of diffractor curvature defects to the total instrumental resolution.
The double crystal bending jig, developed specifically on site for JET, consists of two vertically separated four pillar systems utilising multiple micrometers to cylindrically bend the crystals with relative tilt and rotation control. This assembly, with kinematic positioning, is mounted magnetically within in the vacuum box. The whole assembly can be moved to the laboratory for the bending process, which is described next.

The crystal is clamped near each edge by stainless steel pillars (see FIG. 3 top photo: "Active area"), the front ones are fixed with the outer rear pair being pushed against the back of the crystal surface by means of a series of micrometers for each diffractor. Special attention had to be paid to ensure stability of the curvature over

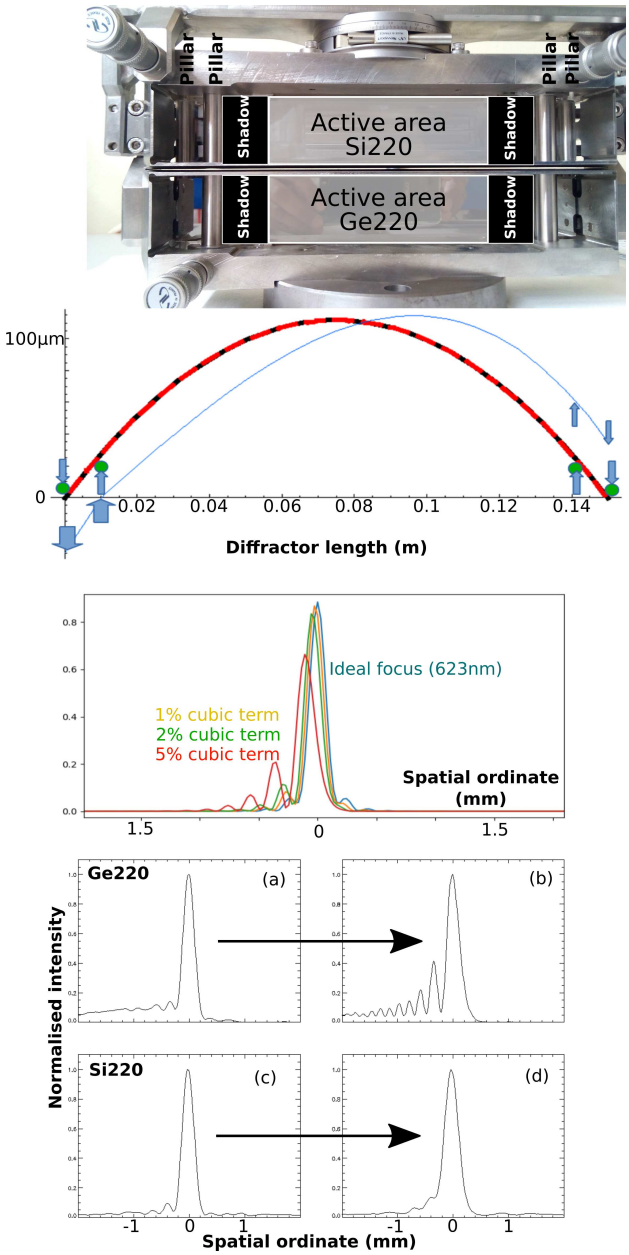

FIG. 3: Diffractor bending jig (top photo) - front pillars can be seen with the x-ray active area clearly shown. Next two figures show the cylindrically-bent focus quality model with a distortion introduced due to asymmetrical pillar movement leading to off-axis structure(s). Actual measurements of Ge and Si spectrometers before (a,c) and after (b,d) the move to the vacuum box are measured in-lab. The Si crystal mechanism is consistently more stable over the move/pump-down procedure.

time. Shifts of $\sim$ 0.1m of the focal position usually occur within 12 hours after the bend exercise. Small excursions also occur during transport to the vacuum chamber, pump-down and the re-measuring procedure of the

focus quality (instrument function) and position – most probably due to thermal excursions and vibrations during kinematic clamping of the jig.
For these exercises a red solid-state laser with small divergence is used behind a 100μm pinhole to ensure that the whole crystal is painted, i.e. is uniformly illuminated by the central region of the Airy disc. A large-area 2D CCD sensor is placed at the focus of the crystal giving a real-time image measurement. The diffractors are locally masked such that only the areas illuminated by x-rays during operation are exposed (see FIG. 3 top photo). The resulting image for the Si crystal assembly is stable when comparing measurements from before and after the jig was transported to/from the kinematic mount in the crystal box and the laboratory. The mechanism was left alone after the best focus was achieved. The measurement of the diffraction pattern is in qualitative agreement with ray-tracing calculations also shown in the FIG 3), where the point spread function is calculated using a ray-tracing program from an ideal cylinder (quadratic) with different levels of (cubic) distortions introduced e.g. from non-symmetrical small movement of the pillar(s).

Low ion temperature assessment

These measurements show that the new Si diffractor has better bend stability than the mainstay Ge one. However this can be used advantageously to determine an upper limit of the Ge instrument function by using emission from the JET plasma itself. Low density, Radio frequency (RF) heated, plasmas have high electron temperatures but low ion temperatures due to the electron-ion equipartition timescales. In such plasmas there is strong emission from both H- and He-like ions of nickel but the Doppler width compared with the instrument function is small. FIG. 4(a) shows the H-like Ni ion temperature (Si diffractor) with He-like Ni ion temperatures (Ge diffractor) as its instrument function width is varied over several fits. The instrument function, now fixed at these lowest ion temperatures, is invariant and will be of less significance for standard plasmas, where ion temperatures are substantially higher where the Doppler component dominates.
The ion temperature is extracted from the line of sight measurement by fitting the spectrum to an emission model and measured instrument function. A local equilibrium balance between the H- and He-like nickel ions is assumed, using measured electron temperature and density profiles. The atomic data for ionization and recombination rates is from ADAS [17] and relative satellite-line intensities follow those of [18]. In FIG. 4(b) the ion temperatures for H- and He-like Ni are shown with their spatial ordinate being the centroid and a single standard deviation calculated from the fit. The figure highlights the fact that that the H- and He-like Ni ion temperatures are in good agreement with other measurement techniques and, for this plasma, with measured electron and temperatures.

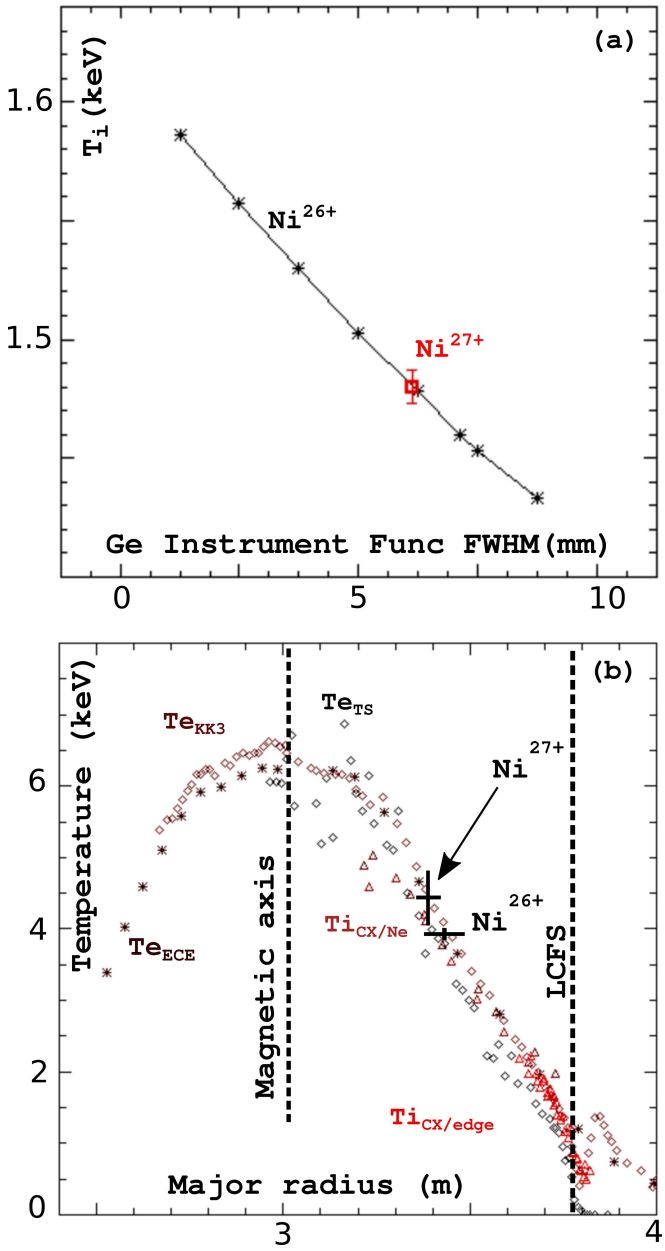

FIG. 4: (a) The low ion temperature limit for the Ge spectrometer can be effectively set by the more stable Si spectrometer mechanism (JET #105613, 11.4-17.4s) due to its stable instrument function, (b) In most JET plasmas the Doppler width dominates: here ion temperatures from the spectrometers show consistency with other data: (JET #105781, 12.5s).T_e is from Thomson scattering (TS) and electron cyclotron emission (ECE, KK3), T_i is from charge-exchange (CX).

Vignetting

As noted here and in [11, 16], the He-like Ni^{26+} emission is firmly at the centre of the Ge220 range and does not suffer any vignetting. However the field of view for the Ni-Ly$_{\alpha_1}$ line does partly span the inner wall boundary area (see FIG. 1). From suitable plasma temperature and density conditions it is possible to select data frames that exclude any line emission across the field of view. An effective vignetting function may then be estimated by analysing continua over many pulses and applied to higher performance plasmas when the line emission is present. The experimentally generated vignetting curve is shown in FIG. 5(a). The rollover at the ends of the

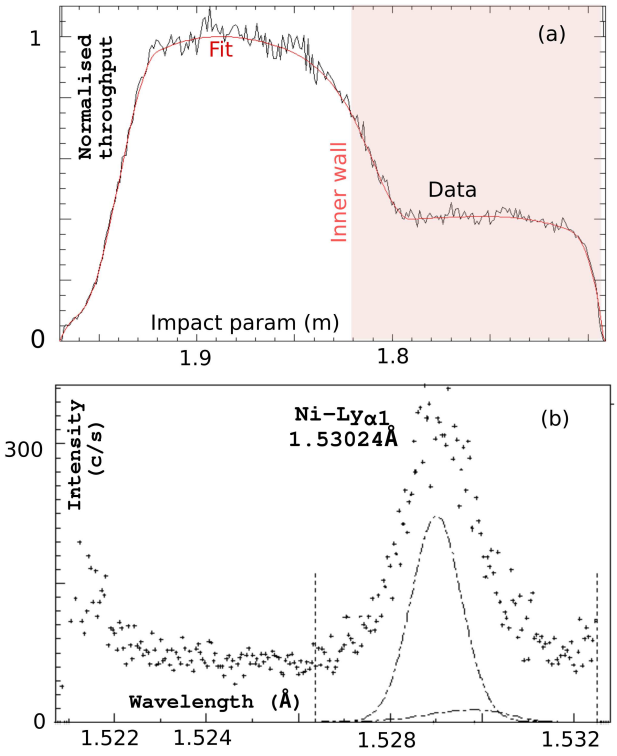

FIG. 5: (a) Vignetting over the centre of the field of view from continua with data frames that are carefully selected to exclude line radiation - namely lower core temperature plasmas where Ni-Ly$_{\alpha 1}$ intensities are negligible. (b) Example application to the H-like Ni-Ly$_{\alpha 1}$ and associated satellites for JET pulse #105775, over the time period 7.7-7.9s, emissivity peak/stddev at r/a=0.3±0.09: $T_i \approx 6.74 \pm 0.6$keV, $T_e = 7.96 \pm 2.94$ keV (T_e from TS ∼8keV for this r/a region). The impact parameter axis shown in (a) is mapped to the wavelength scale in (b).

crystal are due to the line of sight obstructions. The fit to a spectrum with a prominent Ni-Ly$_{\alpha_1}$ and satellites, from a high performance, high electron temperature, plasma shown in FIG 5(b). The main emission and satellite lines fitted shows the importance of accounting for the vignetting.

Spectrometer sensitivity

The sensitivity for a Johann x-ray spectrometer geometry may be expressed as $S = LT\eta$ where T is the system transmission, η the detector efficiency and the luminosity is given by $L = R_c A h_d / 2R$, which is a function of the diffractor reflectivity (R_c), crystal area (A), sensor height (h_d) and the Rowland circle radius (R).
A schematic layout of the spectrometer is given in FIG. 6 showing all the components from the barrier at the JET plasma to the sensor. The optical throughput is the same for both spectrometers apart from the diffractors, an air gap difference due to the relative sensor positions and the Mylar attenuators. These are used to attenuate the brighter first order emission to a level similar to that of the second order so that the sensor may operate optimally below its saturation limit. The alignment of the

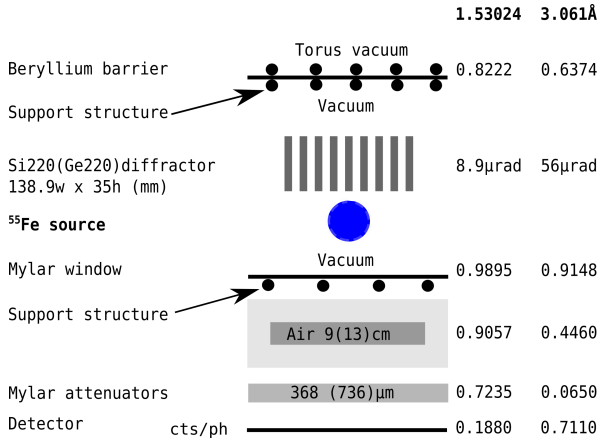

FIG. 6: Schematic of all spectrometer attenuation components. Fractional attenuation at the two energies over the 1^{st} and the 2^{nd} diffraction orders for the Si crystal are also printed. Values in brackets are for the Ge220 spectrometer. The ^{55}Fe source is located in the vacuum and paints all components from that position to the sensors

centres of the sensors, diffractors and barriers is achieved using low-divergence visible lasers and the alignment of the spectrometer both in air and under vacuum has been historically robust. One of the more difficult measurements to make is the transmission fraction of the Mylar attenuators. This is naturally low and because of insufficiently accurate tolerances in the manufacturing process, it is necessary to measure this value on a continuous basis by monitoring an in-situ ^{55}Fe source over the active areas of the sensors. Attenuation at the principal 5.9keV energy is measured and the lower energy value is derived from the properties of Mylar given in the CXRO database (URL: https://henke.lbl.gov/optical_constants/). The sensor efficiency components, for 5 and 12μm Mylar with

0.2μm Al and a 15mm conversion gap operating with a detector gas mixture of 70:30% $ArCO_2$, have been characterised in detail [19] at the operation energies in question, values of which are also shown in FIG. 6 for the Si diffractor spectrometer.

ABSOLUTE THROUGHPUT

For most JET plasmas the He-like lines of nickel cover the Ge spectrometer sensor's width, in both the first and second order. In contrast the H-like Ly_{α_1} line observed by the Si spectrometer is only significant during high-temperature plasmas (> 5keV). Furthermore only one $Ar16^+$ line (≈3.056Å, $1s^2$-1s8p [20]) is present in the spectrum during argon-seeded plasmas. Therefore the Si spectrometer is mostly line-free and is ideal for the study of continua.

Continuum emission from the hydrogen (and its isotopes) fuel and impurities are due to bremsstrahlung (free-free) and radiative recombination (free-bound) processes. The absolute levels of the continuum, over the small wavelength bandpass of the instrument (TABLE I), may be calculated using the measured instrument sensitivity outlined in the previous section. Atomic data for the model is from ADAS (Summers, H. P. (2004), the ADAS User Manual, version 2.6 http://www.adas.ac.uk) with modelled continuum emission following the methods of [21]. The calculations use the measured profiles of the electron temperature and density from the high resolution Thomson scattering diagnostic and the mapping from flux-surfaces to chordal line of sight (EFIT [22]) is needed to evaluate the integrated line of sight predictions.

A strong check on the viability of this method is to consider the special cases where the plasma effective charge Z_{eff}=1, for helium plasmas where Z_{eff}=2 and in seeded argon plasmas where argon emission is significant. In these plasmas the continuum emission can be calculated. The Z_{eff} calculated from the Si spectrometer in first and second order, namely over 3.042-3.066Å (∼8keV) and 1.521-1.533Å (∼4keV) with a shorthand nomenclature of 4/8keV, may be compared to the independent measurement based on emission in the visible part of the spectrum, here termed as VB (Z_{eff} measurements from VB are detailed in [23]).

"Clean" plasmas

The time evolution of the VB (Z_{eff}) measurement compared to that measured and modelled (based on measured density, temperature and line-of-sight flux structure) at the 4keV and 8keV energies for a JET pulse is shown in FIG. 7. The error bar in the time dimension is due to sufficient counting statistics and that of the intensity is a single standard deviation from the fit over that time interval.

Over the steady-state, divertor phase, of the pulse (10-

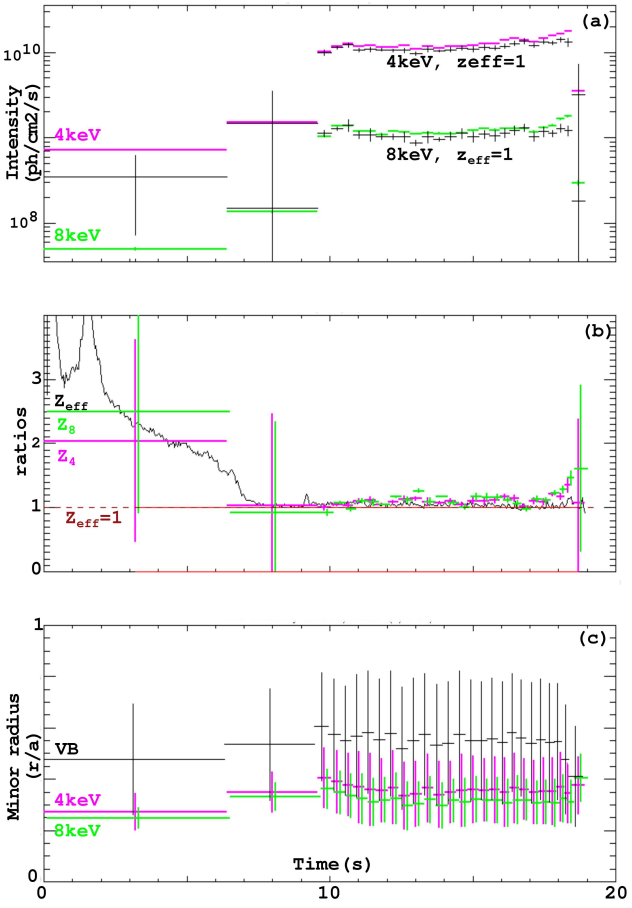

FIG. 7: (a) Si diffractor intensity measurements at the 4/8keV (photon energy) background for JET pulse #96897 and the calculated Z_{eff}=1 bremsstrahlung for the same LOS. (b) Z_4 and Z_8 are ratios of the measured and calculated 4/8keV intensities respectively and here can be effectively considered as equivalent to Z_{eff}. Also shown in (b) is Z_{eff} from VB. (c) Illustrates the extent of VB, 4 and 8keV bremsstrahlung emissivities over r/a: mean with a single standard deviation error bar.

18.5s), Z_{eff} from the VB measurement agrees with the Z_4 and Z_8 ratios (which is effectively Z_{eff} in this minor radius region) derived from the two continua measurements (FIG. 7(b)). Emission from the 4keV and 8keV, being dependent on electron temperature, arises from slightly different locations in the plasma cross-section (FIG. 7(c)). It should be noted that the VB emission also covers a much larger plasma cross-section than the two x-ray emissions. The effective peak and standard deviation of the three measurements is shown in FIG. 7(c) and is calculated following the approach outlined in [24]. The lower end of the spatial line-of-sight localisation is above r/a ∼ 0.2 because the magnetic axis of a JET plasma is above the geometric machine axis since the installation

of the divertor [25] and the x-ray spectrometer remains at its original position viewing the geometric centre.
The agreement between the calculated "synthetic" bremsstrahlung from the two diffraction orders and the VB emission for plasmas essentially free of impurities confirms the method for evaluating the diagnostic component throughput.

Helium plasmas

For JET plasmas with helium as the majority species the effective charge is very close to 2 [26] which can be used as another self-calibration method. FIG. 8 is the

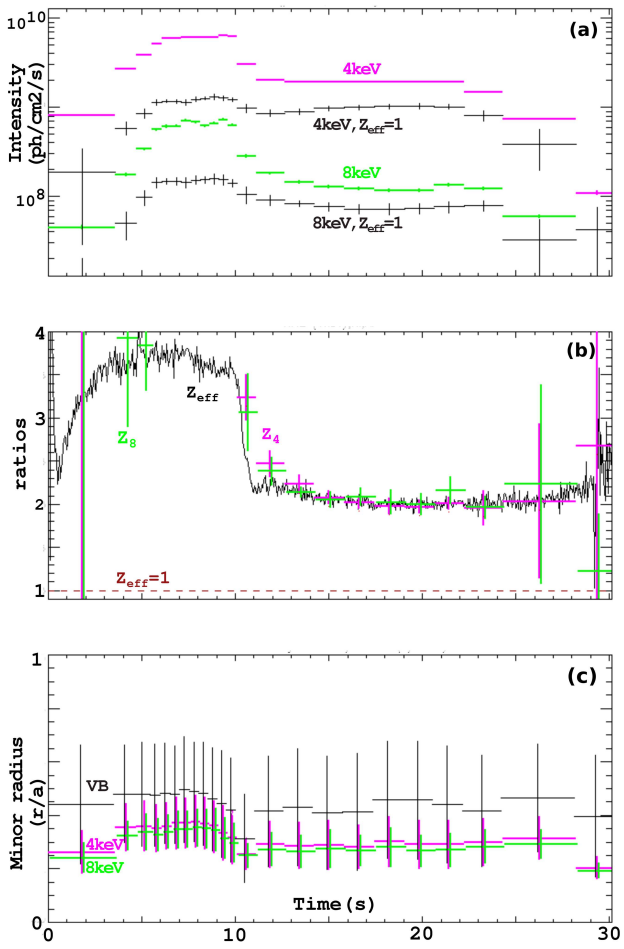

FIG. 8: (JET #97275) Si diffractor intensity levels at the 4/8keV energies and the $Z_{eff} = 1$ calculated intensity as well as the their radial parameters for a helium plasma. Z_{eff} from VB is also shown.

same as FIG. 7 for a Z_{eff}=2 plasma. The same good agreement between the two Si orders and the VB measurement is a further confirmation of the calibration of the x-ray based diagnostic where the temporal evolution of the plasma shape, density and temperature are different. Note that the emission from helium is dominated by free-free bremsstrahlung with little free-bound emission contribution at either the 4keV or 8keV x-ray energies. Here VB, Z_4 and Z_8 are equivalent to Z_{eff}, apart from the spatial extent of respective emissivities.

Argon seeded plasmas

In large tokamaks such as JET, non-intrinsic impurities are used to seed plasmas in order to reduce the power load on divertor and plasma facing components [27]. Generally speaking in plasmas there will also be intrinsic impurities such as beryllium, nickel (from inconel in JET vessel) and tungsten contingent upon interaction of the plasma ans vessel components. All of these will contribute to the continuum spectrum via free-free and free-bound channels. FIG 9 shows these emissivities over the 0.5-10keV photon range at an electron temperature of 2keV for a set of impurities with the quoted concentrations.
The fractional abundance of the ions of each element is that of equilibrium balance with the atomic data, bremsstrahlung and free-bound recombination taken from ADAS.
The concentration of argon in seeded plasmas is much higher than that of other impurities and the continuum emission at 4keV from it will contribute to the total of the emission in these plasmas. It is reasonable to assume that principal contributors: nickel, argon and hydrogen ions, contribute at the 4keV continuum - other intrinsic impurity concentrations are not important judging from the spectral information available. Given the nickel concentration measurements and its contribution to the continuum at 4keV, the argon concentration thus deduced is hence a maximum figure. Furthermore a coronal balance, neglecting the effect of impurity transport, is appropriate since the peak of the x-ray emission originates closer to the core than the edge (see FIG 7(c) and 8(c)) where transport effects are lower [28].

An argon seeded pulse is shown in FIG. 10 where the (maximum) argon concentration and Z_{eff}(D+Ar) are calculated from the x-ray continuum at 4keV where the continuum contribution due to nickel concentration (measured by the Ge spectrometer) is taken away. As mentioned the argon and nickel ions are principal contributors to Z_{eff} for the pulse shown here.
The Z_{eff}(D+Ar) tracks the VB value closely and the Ar concentration lags the injection waveform from the piezo-valve is as expected. From the X-point formation at 6.3s Z_{eff} (D/Ar/Ni) tracks Z_{eff} from VB rather well. Small differences in the Z_{eff} from VB and that due to nickel, argon and the main ion may be due to other impurities such as Be and W and/or due to the spatial coverage of the radiation indicated in FIG. 10(c).

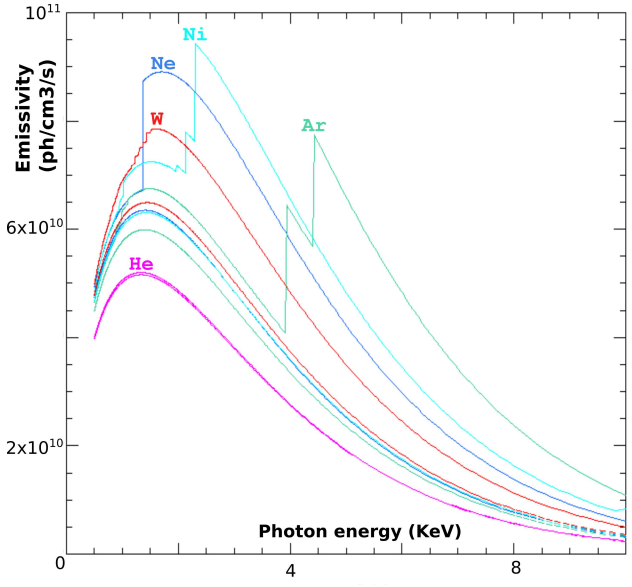

FIG. 9: Free-bound+free-free (upper curves) and free-free emissivities at 2keV electron temperature for principal intrinsic (5%He, 0.03%Ni, 0.015%W) and extrinsic (0.2%Ne, 0.05%Ar) JET impurities.

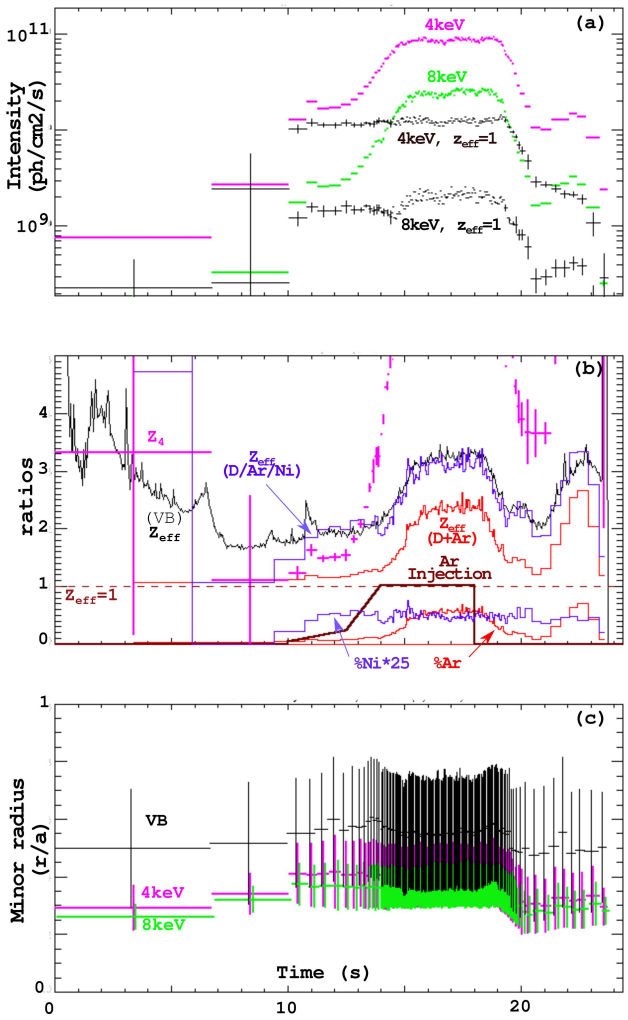

FIG. 10: Details of the Argon-seeded plasma pulse (JET #102598): (a) measured and calculated intensities at 4/8keV energies, (b) Z_4 continuum ratio (magenta), Ar gas injection waveform (brown, normalised), %Ar concentration derived from Z_4 emissivity less the contribution from the measured nickel concentration, resulting Z_{eff} (red) from argon and Z_{eff} (purple) from nickel/argon. Ni concentrations reach ~0.02% and is measured by the Ge spectrometer, and (c) spatial emissivity assuming coronal equilibrium.

Summary

The spectrometer throughput of the JET x-ray spectrometer has been characterised at two narrow spectral bandpasses at 4 and 8keV photon energies. Here the plasma emission consists of free-free and free-bound continuum emission from fuel and impurity components of the plasma. Plasma-Z_{eff} derived from these continua for a "clean" and from a He-ion majority plasmas and have been derived and agrees with chord-integrated Z_{eff} based on VB measurements at the JET geometric equator.
Further, we propose that the intensity for 4/8 keV photons can be used to diagnose concentrations of an externally introduced single impurity. The case highlighted here, an argon-seeded plasma, estimates of the upper-limits to the concentration, and contribution to Z_{eff} shows good though delayed correlation with the introduced gas volume and with plasma-Z_{eff}.
Further work is envisaged to improve the analysis method to other impurity species introduced once or multiple impurities, multiple times in a sequential manner into JET plasmas.
To conclude: an x-ray spectrometer that is sufficiently well aligned using visible lasers and with measured response and throughput of all spectrometer components are key to quantitatively interpret the whole of the collected data across the spectrum. Be it Doppler-broadened line emission or indeed, as demonstrated here, the continuum. In reactor-class tokamaks, x-ray diagnostic-access will be limited as diffractors can be damaged e.g. by intense neutron bombardment. This can be mitigated by the use of neutron-hardened pre-dispersers that deflect x-ray wavelengths of interest to spectrometers: the continuum component of the spectrum may be an invaluable source of information as shown here.

ACKNOWLEDGMENTS

The authors would like to thank S. G. Tyrrell for technical contributions and Dr. J. Mailloux for useful JET physics, DTE2/3 campaign and reactor-relevant diagnostics discussions.
JET, which was previously a European facility, is now a UK facility collectively used by all European fusion laboratories under the EUROfusion consortium. It is operated by the United Kingdom Atomic Energy Authority, supported by DESNZ and its European partners.
This work, which has been carried out within the framework of the Contract for the Operation of the JET Facilities up to 31 October 2021, has been funded by the Euratom Research and Training Programme. Since 31 October 2021, UKAEA has continued to work with the EUROfusion Consortium as an Associated Partner of Max-Planck-Gesellschaft zur Förderung der Wissenschaft e.V represented by Max-Planck-Institut fur Plasmaphysik ("IPP") pursuant to Article 9.1 of the EUROfusion Grant Agreement for Project No 101052200. The views and opinions expressed herein do not necessarily reflect those of the European Commission.

REFERENCES

[1] P. Rebut and B. Keen, Fusion Technology **11**(1), 13 (1987).
[2] C. F. Maggi, Nuclear Fusion **64** (2023).
[3] V. Zotta, L. Garzotti, S. Gabriellini, R. Gatto, C. Bourdelle, C. Giroud, L. Frassinetti, D. Frigione, D. King, D. Keeling, *et al.*, in *50th EPS Conference on Plasma Physics Salamanca, 8th-12th July 2024* (2024).
[4] M. Bitter, S. Von Goeler, S. Cohen, K. Hill, S. Sesnic, F. Tenney, J. Timberlake, U. Safronova, L. Vainshtein, J. Dubau, *et al.*, Physical Review A **29**(2), 661 (1984).
[5] J. Dubau, M. Loulergue, T. Group, *et al.*, Journal of Physics B: Atomic and Molecular Physics **15**(7), 1007 (1982).
[6] J. Dubau and S. Volonte, Reports on Progress in Physics **43**(2), 199 (1980).
[7] R. Bartiromo, F. Bombarda, R. Giannella, S. Mantovani, L. Panaccione, and G. Pizzicaroli, Review of scientific instruments **60**(2), 237 (1989).
[8] H. H. Johann, Zeitschrift für Physik **69**, 185 (1931).
[9] B. Kos, T. Vasilopoulou, S. W. Mosher, I. A. Kodeli, R. E. Grove, J. Naish, B. Obryk, R. Villari, and P. Batistoni, in *EPJ Web of Conferences* (EDP Sciences, 2020), vol. 225, p. 02003.
[10] N. Pablant, Z. Cheng, M. O'Mullane, L. Gao, R. Barnsley, M. Bartlett, M. Bitter, E. Bourcart, G. Brown, M. De Bock, *et al.*, Review of Scientific Instruments **95**(8) (2024).
[11] A. Shumack, J. Rzadkiewicz, M. Chernyshova, K. Jakubowska, M. Scholz, A. Byszuk, R. Cieszewski, T. Czarski, W. Dominik, L. Karpinski, *et al.*, Review of Scientific Instruments **85**(11) (2014).
[12] e. a. D. J. Campbell (2024).
[13] M. Tokar, Nuclear fusion **58**(1), 016016 (2017).
[14] M. Tokar, Nuclear Fusion **58**(9), 096007 (2018).
[15] W. Biel, M. Ariola, I. Bolshakova, K. Brunner, M. Cecconello, I. Duran, T. Franke, L. Giacomelli, L. Giannone, F. Janky, A. Krimmer, R. Luís, *et al.*, Fusion Engineering and Design **179**, 113122 (2022).
[16] R. Bartiromo, R. Giannella, M. Apicella, F. Bombarda, S. Mantovani, and G. Pizzicaroli, Nuclear Instruments and Methods in Physics Research **225**(2), 378 (1984).
[17] C. Nicholas, H. Summers, and M. O'Mullane (2010), URL `https://www.adas.ac.uk/adaseu_site/reports/publ_2.pdf`.
[18] F. Bombarda, R. Giannella, E. Källne, G. Tallents, F. Bely-Dubau, P. Faucher, M. Cornille, J. Dubau, and A. Gabriel, Physical Review A **37**(2), 504 (1988).
[19] J. Rzadkiewicz, W. Dominik, M. Scholz, K. Zastrow, M. Chernyshova, T. Czarski, H. Czyrkowski, R. Dabrowski, K. Jakubowska, L. Karpinski, *et al.*, *Novel Design of Triple GEM Detectors for High-Resolution X-Ray Diagnostics on JET, EFDA-JET-CP(11)07/02*, Tech. Rep. (2011).
[20] J. Rice, F. Sciortino, M. Gu, N. Cao, J. Hughes, J. Irby, E. Marmar, S. Mordijck, M. Reinke, and R. Reksoatmodjo, Journal of Physics B: Atomic, Molecular and Optical Physics **54**(17), 175701 (2021).
[21] A. Burgess and H. P. Summers, Monthly Notices of the Royal Astronomical Society **226**(2), 257 (1987), ISSN 0035-8711, https://academic.oup.com/mnras/article-pdf/226/2/257/2867654/mnras226-0257.pdf, URL `https://doi.org/10.1093/mnras/226.2.257`.
[22] M. Brix, N. Hawkes, A. Boboc, V. Drozdov, S. Sharapov, J.-E. Contributors, *et al.*, Review of Scientific Instruments **79**(10) (2008).
[23] H. Meister, R. Fischer, L. D. Horton, C. F. Maggi, D. Nishijima, A. U. Team, C. Giroud, K.-D. Zastrow, J.-E. Contributors, and B. Zaniol, Review of Scientific Instruments **75**(10), 4097 (2004), ISSN 0034-6748, https://pubs.aip.org/aip/rsi/article-pdf/75/10/4097/19181183/4097_1_online.pdf, URL `https://doi.org/10.1063/1.1787167`.
[24] L. Eriksson, E. Righi, and K. Zastrow, Plasma physics and controlled Fusion **39**(1), 27 (1997).
[25] E. Bertolini, Fusion Engineering and Design **30**(1), 53 (1995), ISSN 0920-3796, URL `https://www.sciencedirect.com/science/article/pii/092037969400401R`.
[26] A. Huber, S. Brezinsek, V. Huber, E. R. Solano, G. Sergienko, I. Borodkina, S. Aleiferis,

A. Meigs, D. Tskhakaya, M. Sertoli, M. Baruzzo, D. Borodin, *et al.*, Physica Scripta **96**(12), 124046 (2021), URL https://dx.doi.org/10.1088/1402-4896/ac2d85.

[27] G. Matthews, B. Balet, J. Cordey, S. Davies, G. Fishpool, H. Guo, L. Horton, M. Von Hellermann, L. Ingesson, J. Lingertat, *et al.*, Nuclear Fusion **39**(1), 19 (1999).

[28] C. Giroud, R. Barnsley, P. Buratti, I. Coffey, M. von Hellermann, C. Jupén, K. Lawson, A. Meigs, M. O'Mullane, A. Whiteford, K.-D. Zastrow, and the JET EFDA contributors, Nuclear Fusion **47**(4), 313 (2007), URL https://dx.doi.org/10.1088/0029-5515/47/4/010.